PHYSICAL REVIEW B **101**, 024422 (2020)

Orbital reconstruction mediated giant vertical magnetization shift and insulator-to-metal transition in superlattices based on antiferromagnetic manganites

Guowei Zhou,[1,2,3,*] Huihui Ji,[1,*] Weinan Lin,[3] Jun Zhang,[1] Yuhao Bai,[2] Jingsheng Chen,[3]
Mingzhong Wu,[4] and Xiaohong Xu[1,2,†]
[1]*School of Chemistry and Materials Science of Shanxi Normal University and Key Laboratory of Magnetic Molecules and Magnetic Information Materials of Ministry of Education, Linfen 041004, China*
[2]*Research Institute of Materials Science of Shanxi Normal University and Collaborative Innovation Center for Shanxi Advanced Permanent Magnetic Materials and Technology, Linfen 041004, China*
[3]*Department of Materials Science and Engineering, National University of Singapore, Singapore 117575, Singapore*
[4]*Department of Physics, Colorado State University, Fort Collins, Colorado 80523, USA*

(Received 16 July 2019; revised manuscript received 26 November 2019; published 24 January 2020)

Heterostructures made of strongly correlated oxides host various fundamentally interesting and potentially useful emergent phenomena. $(\mathrm{LaMnO_3})_n/(\mathrm{SrMnO_3})_{n-1}$ superlattices that consist of an *A*-type antiferromagnetic insulator $\mathrm{LaMnO_3}$ and a *G*-type antiferromagnetic insulator $\mathrm{SrMnO_3}$ were investigated in this work. Several very intriguing effects were observed in such superlattices that include (1) the coexistence of a strong exchange bias effect and a giant vertical magnetization shift in superlattices with intermediate periods, (2) an insulator-to-metal transition associated with a change in the superlattice thickness, and (3) a large nontrivial negative magnetoresistance around the insulator-to-metal transition. To understand these phenomena, microscopic preferential orbital occupancy in different superlattices was studied through measurements of x-ray linear dichroism at Mn *L* edges. This study facilitated the construction of a spin configuration model that takes into account the competition between interfacial ferromagnetism and underlying canted antiferromagnetism in the superlattices and can successfully explain the observed novel magnetic and transport properties. The phase transition and giant vertical magnetization shift phenomena observed in this work offer additional degrees of freedom for applications of antiferromagnetic insulator manganite-based superlattices, enabling novel device concepts.

DOI: 10.1103/PhysRevB.101.024422

I. INTRODUCTION

The rapid development of thin-film growth technologies has allowed the control of layer-stacking structure growth in atomic-sized levels [1]. Such structures include perovskite heterostructures; perovskite layered structures provide a unique platform for the design and engineering of oxide interfaces with the goal of searching for unusual interfacial electronic and magnetic properties that substantially differ from the properties of conventional thin films [2,3]. It has been previously discovered that metallic conductivity can be present at interface between two electrical insulators, such as $\mathrm{LaAlO_3/SrTiO_3}$ and $\mathrm{LaTiO_3/SrTiO_3}$; this discovery represents a milestone in studies of heterostructure interfaces [4,5].

In the family of perovskite manganites, $\mathrm{LaMnO_3}$ (LMO) with nominal $\mathrm{Mn}^{3+}t_{2g}^3e_g^1$ occupancy is an insulator with strong Mott-Hubbard or charge-transfer Coulomb correlations in a half-filled e_g band and shows an *A*-type orbital-ordered antiferromagnetic (AFM) behavior at low temperatures [6]; $\mathrm{SrMnO_3}$ (SMO) with $\mathrm{Mn}^{4+}t_{2g}^3e_g^0$ occupancy is a band insulator with a *G*-type or cubic AFM order [7]. Through dynamical mean-field theory calculation, Lin *et al.* predicted that the LMO/SMO interface is analogous to the LTO/STO system and should have a ferromagnetic metal state governed by double-exchange hopping of e_g electrons [8]. And, the transport and magnetic properties of large-period LMO/SMO superlattices have been researched rather intensively through experiments by scientists in recent years [9–20]. In particular, it has been found that the LMO/SMO superlattices show the electrical and magnetic behaviors of bulk $\mathrm{La_{0.7}Sr_{0.3}MnO_3}$ (LSMO) for very thin LMO and SMO layers ($n = 1-2$ unit cells), but host an insulating ground state for thicker layers ($n \geqslant 3$) [12]. Further, a large magnetoresistance (MR) effect has been reported for the insulating ground state; it has been conjectured that this MR effect originates from the coexistence of the ferromagnetic (FM) and antiferromagnetic phases [17]. However, it is still an open question whether the AFM and FM phases actually coexist and how they affect or depend on each other.

It is known that one can make use of the exchange bias effect (EBE) to characterize the magnetic configuration of the materials and check whether FM and AFM phases coexist. The EBE is usually characterized by an asymmetric shift in the magnetic hysteresis loop along the field axis after an FM/AFM layered or composite system is cooled in a static magnetic field through the Néel temperature of the AFM component. The inevitable outcomes of the exchange interaction are usually identified as either the horizontal loop shift

---

[*] These authors contributed equally to this work.

[†] Corresponding author: xuxh@sxnu.edu.cn

or the coercivity enhancement [21]. Surprisingly, a vertical magnetization shift (VMS) coexisting with the conventional horizontal shift has been observed recently in the epitaxial bilayer of the itinerant FM $SrRuO_3$ and the *G*-type AFM $La_{0.3}Sr_{0.7}FeO_3$ [22,23]. The VMS response, i.e., the offset of the hysteresis loop along the magnetization axis, has rarely been detected experimentally [24–34]. The conjunction of the EBE with the VMS is a very interesting phenomenon because it offers an additional degree of freedom that can be harnessed in future spintronic device applications. As a consequence, in recent years considerable research efforts have been initiated to explore the key aspects of the new VMS phenomenon [32]. Of particular note is that polarized neutron reflectivity measurements indicate that the occurrence of the EBE and the VMS can be attributed to both the FM and the AFM layers [35]. In spite of those efforts, however, it is still natural to ask whether this phenomenon is universal; it is still an open question whether the EBE and the VMS can coexist in LMO/SMO superlattices.

Here we report surprising transport and magnetic properties in superlattices that consist of *A*-type AFM insulator LMO and *G*-type AFM insulator SMO sublayers, with the layer thickness chosen delicately. A metal-to-insulator transition due to the increase of the sublayer thickness is observed at low temperatures. In LMO/SMO superlattices with intermediate periods, the coexistence of strong EBE and VMS responses as well as large negative magnetoresistances are observed. Through x-ray linear dichroism (XLD) measurements at the Mn *L* edges, the orbital reconstruction is detected with an increase in the superlattice thickness. Following the comprehensive analysis of the XLD results, a spin configuration model is proposed that takes into account complex competition between interfacial ferromagnetism and the underlying canted antiferromagntism in the superlattices. This model is supported by control measurements and can be used to explain the observed transport and magnetic properties.

II. EXPERIMENTAL DETAILS

Sample preparation. Fully epitaxial superlattices of $[(\mathrm{LMO})_n/(\mathrm{SMO})_{n-1}]_t$, where n and t were integers of unit cells (u.c.) and their product was kept constant at 40 (except for $n = 3$, $t = 13$), were deposited on atomically flat $SrTiO_3$ (001) substrates by pulsed laser deposition (PLD) techniques. For the sake of convenience, the superlattices of LMO/SMO studied in this work are denoted as L_nS_{n-1} in the following. All the superlattices had LMO as the top terminating layer. The L_nS_{n-1} superlattices with $n \leqslant 2$, $3 \leqslant n \leqslant 5$, and $n > 6$ are denoted as short-period, intermediate-period, and long-period superlattices, respectively, in the following. Prior to the deposition, the substrates were etched with buffered HF acid. During the deposition, the *in situ* reflection high-energy electron diffraction (RHEED) was used to monitor the quality of L_nS_{n-1} superlattices. The distance between the substrate and the target was kept constant at 75 mm. The samples were grown using a 248 nm KrF excimer laser with a frequency of 2 Hz, at a temperature of 725 °C, and under an oxygen pressure of 100 mTorr. To avoid oxygen vacancies, which can cause anomalous metallic behavior through electron doping, the superlattices were annealed *in situ* for 1 h under an oxygen pressure of 300 Torr. For comparison, $La_{0.7}Sr_{0.3}MnO_3$ (20 u.c.), LMO (40 u.c.), and SMO (30 u.c.) thin films were also grown under the same experimental conditions as for the growth of the L_nS_{n-1} superlattices. Further details on the superlattice growth were provided in Ref. [36].

Structural characterization. The crystalline orientations of the LMO/SMO superlattices were characterized by conventional x-ray diffraction (XRD) techniques. To characterize the epitaxial structure quality and interface sharpness of the superlattices, the scanning transmission electron microscope (STEM) measurements using a high-angle annular dark field (HAADF) were performed on a Titan 80-300 microscope (FEI) equipped with an aberration corrector. This setup was used at 300 kV acceleration voltages for imaging with a 20 mrad convergence angle and a collection angle of 40–95 mrad. The in-plane magnetic measurements were performed with a vibrating sample magnetometer in a physical propertiy measurement system (PPMS-VSM); the out-of-plane hysteresis loops were measured in a superconducting quantum interference device (SQUID) over a temperature range of 5–360 K. The hysteresis loops were obtained after subtracting the diamagnetic background of the STO substrates and the plastic tube. The electrical transport measurements were performed using a van der Pauw four-probe configuration with the Quantum Design PPMS in a temperature range of 5–360 K.

Synchrotron measurement. The x-ray absorption spectroscopy (XAS) measurements of the Mn *L* edge in the superlattices were performed at the beamline BL08U1A station of the Shanghai Synchrotron Radiation Facility (SSRF) and the beamline BL12B-a of the National Synchrotron Radiation Laboratory (NSRL). The background vacuum level was 9×10^{-7} Torr, and the absorption signal was detected by the total electron yield (TEY) technique. The spectra were normalized so that the L_3 pre-edge and the L_2 post-edge have coincident intensities for the two polarizations. After that, the pre-edge spectral region was set to zero, and the peak at the L_3 edge was set to 1. The x-ray linear dichroism (XLD) is defined as the difference in the XAS measurements with horizontal ($E \parallel a$) and vertical ($E \parallel c$) polarizations.

III. RESULTS AND DISCUSSION

Figure 1(a) shows schematically the configuration of the $[(\mathrm{LMO})_n/(\mathrm{SMO})_{n-1}]_t$ superlattices studied in this work, with LMO being the top terminating layer. It is generally accepted that LMO bulk materials exhibit an *A*-type AFM ground state, but the FM insulating behavior can be present in LMO thin films. The origin of the ferromagnetism in the thin films is still under debate, although vacancies and strain have been proposed as possible origins. In LMO films thinner than 10 u.c., however, the ferromagnetism is very weak [37]. In order to achieve similarly weak ferromagnetism in the LMO layer, the thickness (n) of the LMO layer was kept in the 2–8 u.c. range and the cycle (t) of the superlattices was varied from 20 to 5.

Figure 1(b) presents the partial RHEED oscillating curve during the growth process, together with the images of diffraction patterns for the bare substrate (top left) and the L_4S_3 superlattice (top right). The clear large-amplitude oscillation and the clear diffraction spots and streaks of the L_4S_3

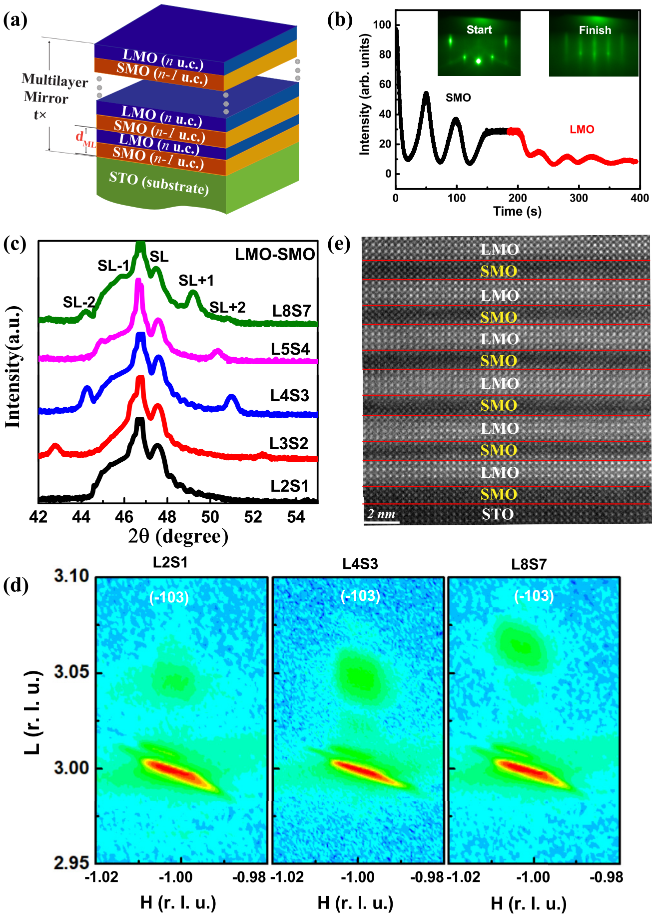

FIG. 1. (a) Schematic view of epitaxial $(\mathrm{LMO}_n/\mathrm{SMO}_{n-1})_t$ superlattices on a (001)-oriented STO substrate. (b) A partial RHEED oscillation curve of the specular beam during the growth of the LMO (4 u.c.)/SMO (3 u.c.) superlattice on a (001) STO substrate. The insets are *in situ* RHEED patterns before and after the deposition. (c) X-ray $\theta-2\theta$ scan around the (002) diffraction peak for five $\mathrm{L}_n\mathrm{S}_{n-1}$ superlattices grown on STO substrates. The first-order superlattice reflections are denoted as SL ± 1. (d) X-ray RSMs from $\mathrm{L}_2\mathrm{S}_1$, $\mathrm{L}_4\mathrm{S}_3$, and $\mathrm{L}_8\mathrm{S}_7$ superlattices around the $(\bar{1}03)$ Bragg diffraction of the STO substrates. (e) An atomically resolved HAADF-STEM image for the $\mathrm{L}_4\mathrm{S}_3$ superlattice.

superlattice evidently indicate layer-by-layer epitaxial growth during the entire deposition process. Although not shown here, the growth of other $\mathrm{L}_n\mathrm{S}_{n-1}$ superlattices was also monitored by *in situ* RHEED to ensure the epitaxial growth.

Figure 1(c) shows representative XRD spectra measured with Cu-K_α radiation around the (002) peaks of the STO substrate for five $\mathrm{L}_n\mathrm{S}_{n-1}$ superlattice samples. The spectra show clear Laue fringes that provide the evidence for the flatness of the superlattices. The satellite peaks SL ± 1 are observed except for the $\mathrm{L}_2\mathrm{S}_1$ sample. The presence of those peaks indicates that the $\mathrm{L}_n\mathrm{S}_{n-1}$ superlattices have smooth interfaces. The 2θ degrees of the SL + 1 peak increase as the thickness of the superlattice decreases, which is expected for Bragg reflections. The high-quality epitaxial structure of the $\mathrm{L}_n\mathrm{S}_{n-1}$ superlattice samples was further verified by x-ray reciprocal space maps (RSMs) around the $(\bar{1}03)$ Bragg peak positions. The RSM is a powerful method to quantify the strain state, which can be identified by the intensity distribution in the vicinity of the detected Bragg peak. As shown in Fig. 1(d), the characteristic $(\bar{1}03)$ diffraction peaks from the $\mathrm{L}_2\mathrm{S}_1$, $\mathrm{L}_4\mathrm{S}_3$, and $\mathrm{L}_8\mathrm{S}_7$ superlattices align vertically with the STO substrates, indicating the coherent strained growth without any lattice relaxation.

To further support the claims of coherent epitaxial growth and the absence of interfacial diffusion in the $\mathrm{L}_n\mathrm{S}_{n-1}$ superlattices, an atomically resolved high-angle annular dark field scanning transmission electron microscopy (HAADF-STEM) image is shown in Fig. S1 of the Supplemental Material [38]. The $\mathrm{L}_4\mathrm{S}_3$ superlattice is selected for the HAADF-STEM measurement, and the image is shown in Fig. 1(e). Layers with atomically flat interfaces can be easily identified in this image. As discussed in a previous report [39], the image intensity is directly proportional to the atomic number. Thus, in Fig. 1(e) the brighter features correspond to the LMO layers, while the darker spots correspond to the SMO layers. Note that the atomic numbers of La and Sr are 57 and 38, respectively. The high quality of the LMO/SMO superlattice structures indicated by the data in Fig. 1 allowed us to explore the magnetic and transport properties of the superlattices, which are presented below.

The transport and magnetic properties of $(\mathrm{LMO})_{2n}/(\mathrm{SMO})_n$ superlattices in comparison with the perovskite $\mathrm{La}_{2/3}\mathrm{Sr}_{1/3}\mathrm{MnO}_3$ alloy films have been studied previously [12]. Short-period $\mathrm{L}_{2n}\mathrm{S}_n$ superlattices are FM metals, while long-period $\mathrm{L}_{2n}\mathrm{S}_n$ superlattices exhibit ferromagnetism only at the interface. In this work, in contrast, the transport and magnetic properties are studied on the $\mathrm{L}_n\mathrm{S}_{n-1}$ superlattices. Figure 2(a) shows the temperature (T) dependence of the resistance for a series of $\mathrm{L}_n\mathrm{S}_{n-1}$ superlattice samples and an LSMO (20 u.c.) film reference sample over a temperature range of 5–360 K. Note that the sample names are indicated in Fig. 2(c), but not in Fig. 2(a) due to space limitation. At the lowest temperature, the resistance increases by over 7 orders of magnitude when n is increased from 2 u.c. to 8 u.c. This clearly shows a thickness-associated metal-to-insulator transition. The transport property of the short-period $\mathrm{L}_2\mathrm{S}_1$ superlattice is quite similar to that of the LSMO film. The kinks in the resistance curves correspond to the ferromagnetic-to-paramagnetic phase transition near the Curie temperature (T_C), as discussed shortly. To better demonstrate this phase transition, we plotted the $d\rho/dT$ versus temperature curves in the inset of Fig. 2(a). It can be seen that the T_C is 275 K for the $\mathrm{L}_2\mathrm{S}_1$ superlattice and 314 K for the LSMO film. Moreover, the intermediate-period $\mathrm{L}_3\mathrm{S}_2$ and $\mathrm{L}_4\mathrm{S}_3$ superlattices undergo the insulator-metal-insulator transition as the temperature increases, as shown in Fig. 2(a) and in Fig. S2(c) of the Supplemental Material [38]. This transition may be associated with the complex magnetic structure in the superlattices. With a further increase in n, the long-period $\mathrm{L}_n\mathrm{S}_{n-1}$ superlattices evidently show an insulator-type transport behavior.

Figure 2(b) shows the magnetoresistance (MR) measured in a perpendicular magnetic field at $T = 5$ K. Here the MR is defined as $[R(H) - R(0)]/R(0)$, where $R(H)$ and $R(0)$ are the resistance values measured in the presence of a magnetic field H and in the absence of a field, respectively. One can see that all the samples show negative magnetoresistances. The insulating $\mathrm{L}_4\mathrm{S}_3$ superlattice shows the largest negative MR

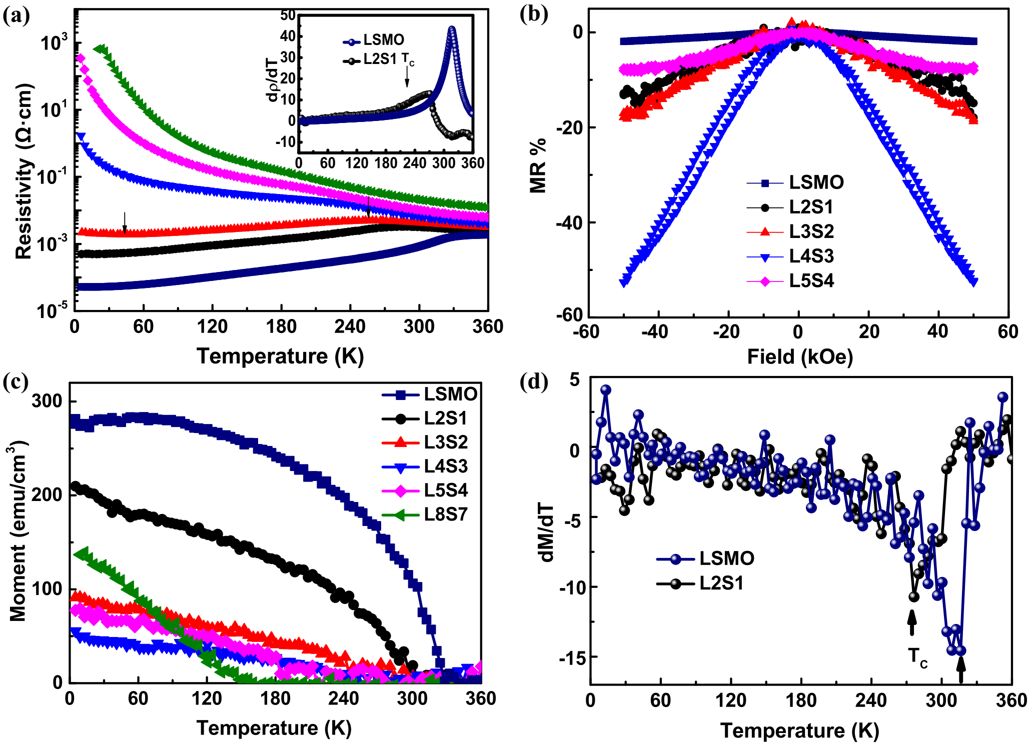

FIG. 2. (a) Temperature dependence of the resistance of a series of L_nS_{n-1} superlattice samples and the LSMO film reference sample. The inset shows the corresponding dR/dT versus temperature curves for the L_2S_1 superlattice and the LSMO film. (b) Magnetic field dependence of the resistance for a series of L_nS_{n-1} superlattice samples (except for L_8S_7) and the LSMO film at 5 K. (c) Magnetic moments of the superlattice samples and the LSMO film measured as a function of temperature with an in-plane magnetic field of 0.5 kOe. (d) dM/dT versus temperature curves for the L_2S_1 superlattice and the LSMO film.

value, which is 58%. This MR value is 5 times larger than that of the metallic L_2S_1 superlattice at 50 kOe. What is more, the MR data show no saturation behavior. The negative MR is generally attributed to the magnetic-field-induced suppression of the coherent interference involved in weak localization. The large MR in the L_4S_3 superlattice may result from the competition between the ferromagnetism at the interface and the interlayer antiferromagnetism as discussed previously [17]. The evidence for the proximity of the AFM/FM regions is the presence of the magnetic pinning in the L_4S_3 superlattice; we will address this point in detail in the next section. Two notes should be made about the MR data. First, the resistance of the L_8S_7 sample at 5 K is too high to be measured accurately and is therefore not presented in Fig. 2(b). Second, the metallic L_2S_1 superlattice and the alloy LSMO film have smaller MR values at 5 K, but they show notable MR at the metal-to-insulator transition temperature, as shown in Fig. S2 of the Supplemental Material [38].

Figure 2(c) gives the magnetic moments as a function of temperature for the same samples for which the resistance data are shown in Fig. 2(a). The data of the $n = 2$ superlattice sample show an FM behavior which is very similar to that of the alloy LSMO film. Figure 2(d) gives the dM/dT versus temperature data for the $n = 2$ superlattice and the alloy LSMO film. The data indicate $T_C = 277$ K for the L_2S_1 superlattice and $T_C = 317$ K for the LSMO film. These two T_C values agree very well with the above-cited values indicated by the resistance data in Fig. 2(a); this consistency clearly shows the magnetic-electrical correlation. The fact that T_C in the L_2S_1 sample is lower than that in the LSMO film may be attributed to the enhanced local disorder at the interfaces. Thus, one can conclude that the short-period L_2S_1 superlattice has transport and magnetic properties similar to those of the alloy LSMO film.

It should be noted that the transport properties of LMO/SMO superlattices have been previously investigated as a function of the superlattice period, and the large negative MR has also been previously observed in intermediate-period superlattices. However, the unambiguous magnetic structures and the exchange bias effect in L_nS_{n-1} superlattices are still unknown. Taking into account this fact, we examined the magnetization-field (M-H) hysteresis behaviors for a series of L_nS_{n-1} superlattices. Figures 3(a)–3(e) present the main data, which were measured after the samples were cooled from room temperature with in-plane magnetic fields of ±50 kOe. It is evident that the direction of the horizontal loop shift is opposite to that of the cooling field for all the samples. This result suggests the presence of the exchange bias effect (EBE) in the L_nS_{n-1} superlattices. The value of the exchange bias field can be determined as $H_{\mathrm{EB}} = |H_+ + H_-|/2$, and the coercive field can be evaluated as $H_C = |H_+ - H_-|/2$, where H_+ and H_- denote the right and left values of the coercivity, respectively.

However, in the intermediate-period L_3S_2, L_4S_3, and L_5S_4 superlattices, the saturation magnetization (M_S) is much larger on the positive-field side than on the negative-field side

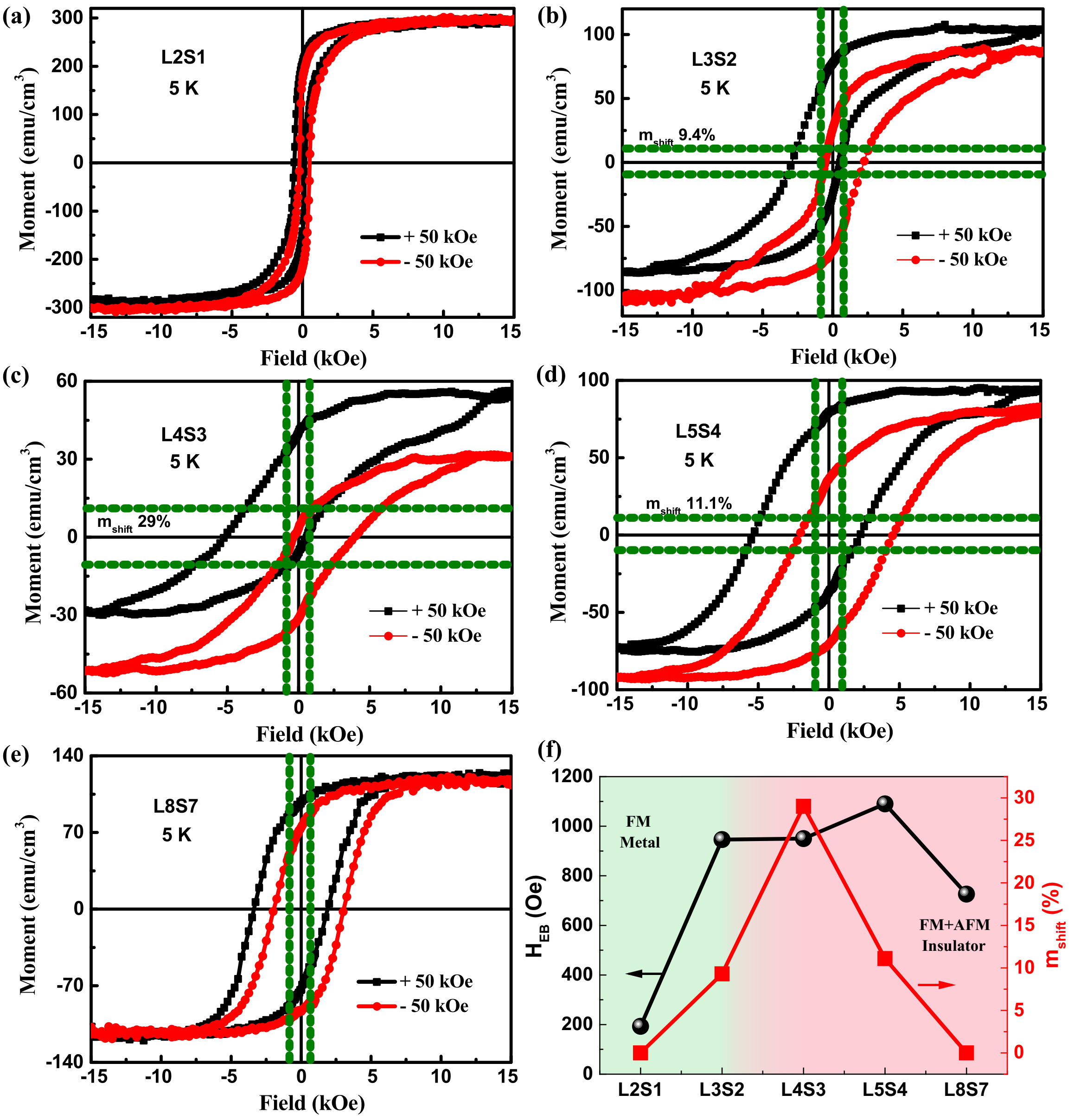

FIG. 3. Magnetic hysteresis loops measured at $T = 5$ K after cooling from room temperature under different in-plane fields (±50 kOe) for (a) L_2S_1, (b) L_3S_2, (c) L_4S_3, (d) L_5S_4, and (e) L_8S_7. The green dashed lines are added for better visualization of the loop shifts. (f) H_{EB} (left axis) and m_{shift} (right axis) of L_nS_{n-1} superlattices, with the thickness n varying from 2 u.c. to 8 u.c.

when the sample is cooled in a positive field; similarly, the magnitude of M_S is much larger on the negative-field side when the sample is cooled in a negative field. These results clearly suggest that the directions of the horizontal shift along the field axis and the vertical shift along the magnetization axis are both determined by the direction of the cooling field for the three samples. The shift of the center of the hysteresis loop along the magnetization axis can be calculated as $m_{shift} = (M_S^+ + M_S^-)/(M_S^+ - M_S^-)$, where M_S^+ and M_S^- are the positive and negative saturation values of the hysteresis loop, respectively [32]. The vertical shift (m_{shift}) value of the L_3S_2, L_4S_3, and L_5S_4 superlattices is 9.4%, 29%, and 11.1%, respectively.

The dependence of the exchange bias effect and the vertical magnetization shift (VMS) on the thickness of L_nS_{n-1} superlattices is shown in Fig. 3(f). Such EBE-VMS coexistence is rare and intriguing; it further supports the presence of strong interaction between the FM order at the interface and the underlying AFM order which is indicated by the above-presented large negative MR value. It should be noted that large VMS effects have been observed in other non-heterostructures, such as polycrystal line ceramics and nanoparticles; in that case, the VMS effect is associated with different mechanisms, including incomplete reversal of the FM spins, or the frozen, uncompensated spins in the spin-glass-like phase at FM/spin-glass interfaces [40–42]. Further, in AFM/FM heterostructures such as $SrMnO_3/SrRuO_3$ superlattices and $La_{0.7}Sr_{0.3}FeO_3/SrRuO_3$ bilayers, the VMS effects have been observed previously; they are associated with pinned moments and uncompensated

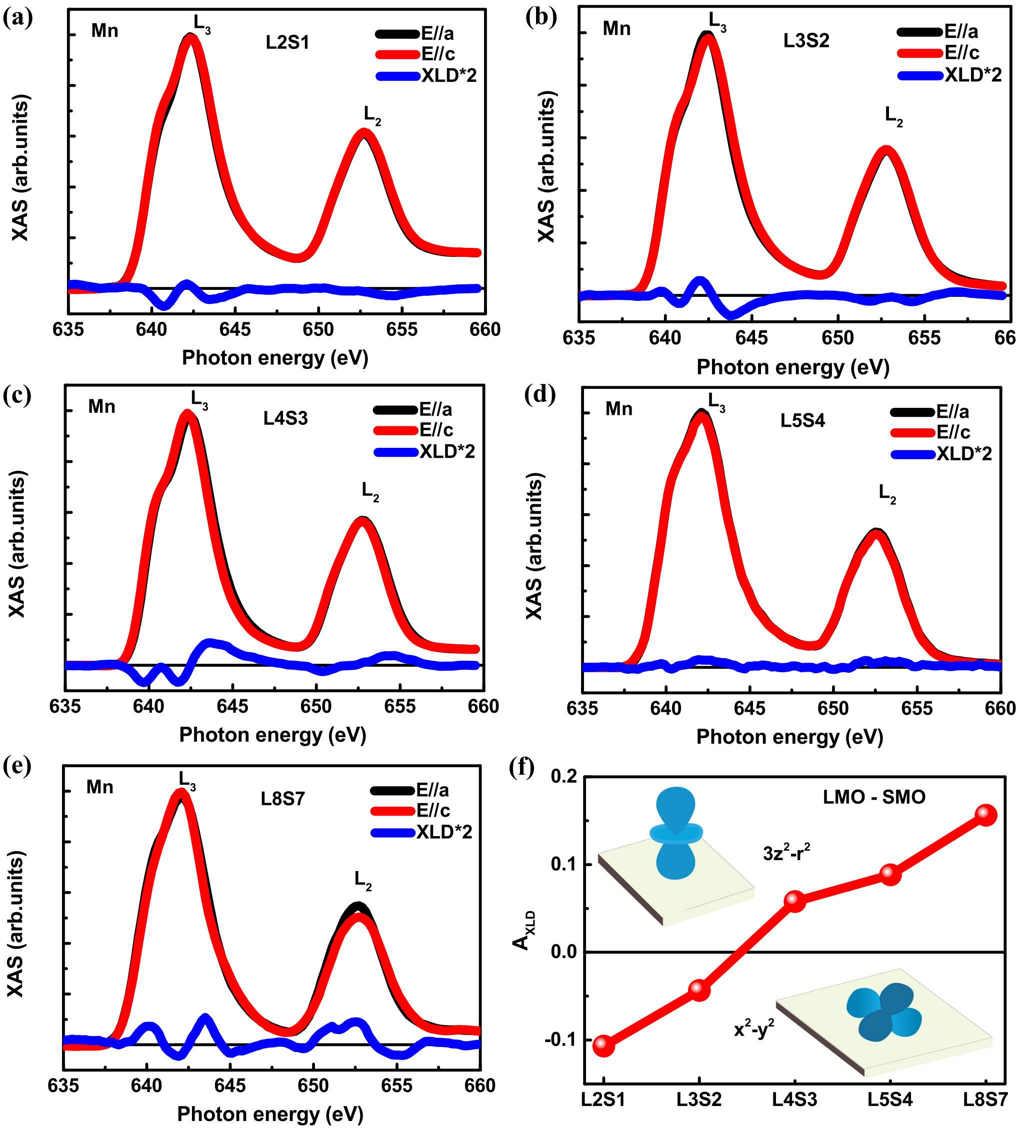

FIG. 4. (a)–(e) Normalized XAS and XLD spectra measured at room temperature with linearly polarized light for a series of L_nS_{n-1} superlattices. The XLD spectra are determined as the difference of the XAS measurements with vertical and horizontal polarizations in a grazing incidence configuration and are normalized to the sum of the XAS L_3 peak height signals. (f) Integral area of the XLD peaks for the five L_nS_{n-1} superlattice samples whose XLD spectra are shown in panels (a)–(e) with the thickness n varying from 2 to 8 u.c.

spins at the interfaces [23,43]. In contrast, the mechanism for the EBE-VMS coexistence in the LMO/SMO (AFM/AFM) superlattices is still unknown; it is explored in the section below.

It is known that in perovskite transition-metal oxide heterostructures, strong correlations between the charge, spin, and orbital degrees of freedom at the interfaces play a key role in tuning the transport and magnetic properties. It has been previously proved that at an ideal LMO/SMO interface, charge leakage between e_g states on the neighboring Mn^{3+}/Mn^{4+} sites depends on the alignment of the Mn spins via double exchange. The length scale for such charge leakage at the interfaces is estimated to be about 1–2 u.c. [15]. Therefore, the transport and magnetic properties in the short-period L_2S_1 superlattice are quite similar to the alloy LSMO film, while for large periods ($n \geqslant 3$), the superlattice is an insulator consisting of FM/AFM competitive regions. The accurate spin configurations of the FM and AFM phases in the LMO/SMO superlattices are unclear currently. Due to the presence of the spin-orbital coupled states in manganites, the spin textures of the FM and AFM phases along with the preferred e_g level orbital occupation in the large-period L_nS_{n-1} superlattices can be evaluated by synchrotron techniques. The preferential orbital occupation can be measured by x-ray linear dichroism (XLD), a method which relies on the excitation of core electrons into the valence d orbitals by linearly polarized photons. Aruta *et al.* have used the XLD method to successfully analyze the preferential orbital occupancy in LMO_{2n}/SMO_n superlattices [14]. The XLD signal can be obtained from the intensity difference ($I_{ab} - I_c$) between the XAS signals measured with in-plane ($E \parallel a$) and out-of-plane ($E \parallel c$) components [44,45]. To minimize the influence of the magnetic order on the orbital occupancy in the XLD signals, the spectra are measured at room temperature

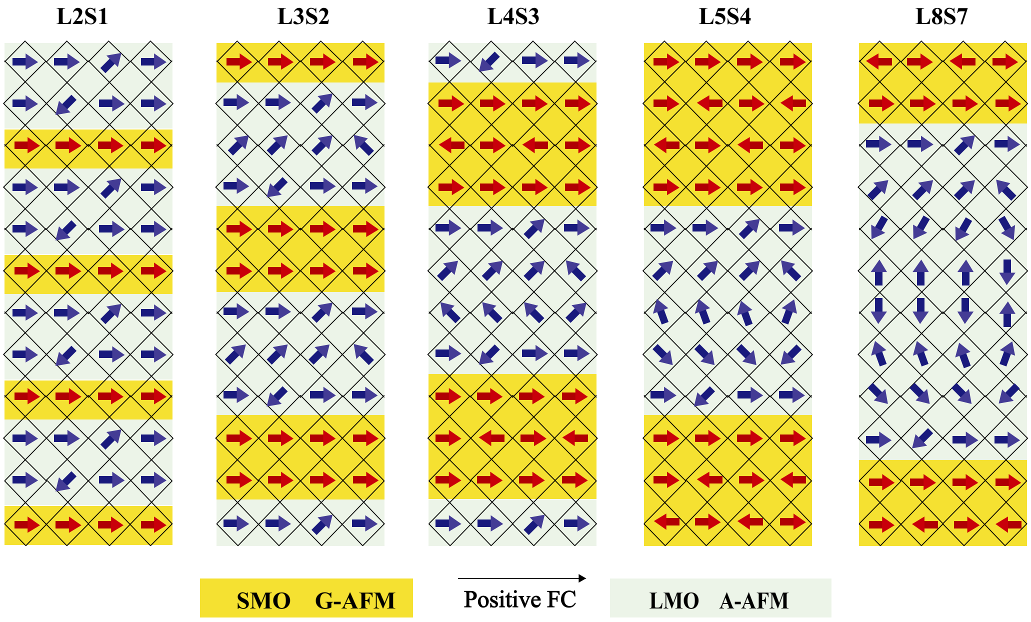

FIG. 5. Schematic diagrams of local spin orientations in different L_nS_{n-1} superlattices after cooling from room temperature to 5 K under a magnetic field of +50 kOe. The dark yellow and cyan colors in the L_nS_{n-1} superlattices denote the *G*-AFM SMO layers and the *A*-AFM LMO layers, respectively.

for all the superlattices. Here, we select the region around the L_2 edge (648–660 eV) to calculate the area A_{XLD} using the method of integration; this area represents the difference between the relative occupancies of the $3z^2-r^2$ and x^2-y^2 orbitals. Positive and negative A_{XLD} values are attributed to a preferential occupancy of the out-of-plane $3z^2-r^2$ orbital and the in-plane x^2-y^2 orbital, respectively. It is worth noting that the orbital contribution to the XLD signal in the L_nS_{n-1} superlattices is mainly given by the LMO layer, because in these superlattices the Mn sites in the SMO layer are essentially $3d^3$, a configuration that is spherical and cannot contribute significantly to the XLD signal.

Figure 4 presents the XLD spectra of the L_nS_{n-1} superlattices around the Mn $L_{3,2}$ edge along with the corresponding in-plane and out-of-plane XAS spectra. For $n = 2$ and $n = 3$, the A_{XLD} has a negative value, as can be seen in Figs. 4(a) and 4(b). This means that the x^2-y^2 orbital is energetically more favorable than the $3z^2-r^2$ orbital. This occurs as a consequence of the tensile strain in the superlattices arising from the lattice mismatch with the STO substrates. However, for $n \geqslant 4$, A_{XLD} shows a positive value, as can be seen in Figs. 4(c)–4(e). This indicates a preferential orbital occupancy of the $3z^2-r^2$ orbital, and the latter results from the interfacial compressive strain in the LMO layer due to the increased SMO layer thickness. Therefore, the orbital reconstruction takes place in the L_nS_{n-1} superlattices with an increase in the thickness n. A summary of the A_{XLD} values for different superlattices is given in Fig. 4(f); this summary highlights the transition of the orbital occupancy from the x^2-y^2 orbital to the $3z^2-r^2$ orbital with an increase in n from 2 u.c. to 8 u.c. Aruta *et al.* have reported that the preferential orbital occupation is of the x^2-y^2 type for thinner n and of the $3z^2-r^2$ type for n thicker than 5, which is similar to our XLD results [14].

Based on the analyses of the in-plane *M-H* loops and the preferential orbital occupation, we can obtain the spin configurations after different field-cooling processes. Figure 5 and Fig. S4 of the Supplemental Material [38] show the schematic diagrams of these spin configurations. For the L_2S_1 superlattice, the magnetic easy axis is in-plane, the preferential orbital occupation is the in-plane x^2-y^2 orbital, and the transport property is metallic due to the interfacial double-exchange effect. Therefore, the spin directions are mainly in-plane oriented due to the interfacial FM anisotropy. In comparison with the alloy LSMO film, the L_2S_1 superlattice has a weaker exchange bias effect, a smaller saturation magnetization, and a lower Curie temperature. As a result, a slightly canted spin configuration should exist in this superlattice.

For the L_8S_7 superlattice, the in-plane and out-of-plane hysteresis loops are shown in Fig. S5 of the Supplemental Material [38]. It is evident that the magnetization easy axis has a tendency toward the out-of-plane direction. At the same time, the preferential orbital occupation is of the $3z^2-r^2$ type. However, the spin configurations at the interfaces are still mainly in-plane oriented and are ferromagnetic. In other words, the LMO component in the superlattice consists of an *A*-type AFM "bulk" with out-of-spin orientation sandwiched by interfacial FM layers. In the SMO layer, the spin configurations are still *G*-type antiferromagnetic. This result also supported by Aruta *et al.* [14].

For the other three intermediate L_nS_{n-1} superlattices, with an increase in the period the preferential orbital occupation transfers from the in-plane x^2-y^2 to the out-of-plane $3z^2-r^2$, resulting in different spin-canting configurations. As shown by the above-presented *M-H* loop data, the EBE and the VMS coexist in the intermediate-period L_3S_2, L_4S_3, and L_5S_4 superlattices. The FM state is expected to be induced at the interface for all LMO/SMO superlattices, as discussed previously [11,12]. The canted AFM states in the LMO layer are induced by the thickness dependence of the orbital reconstruction. Consequently, the FM state at the interface

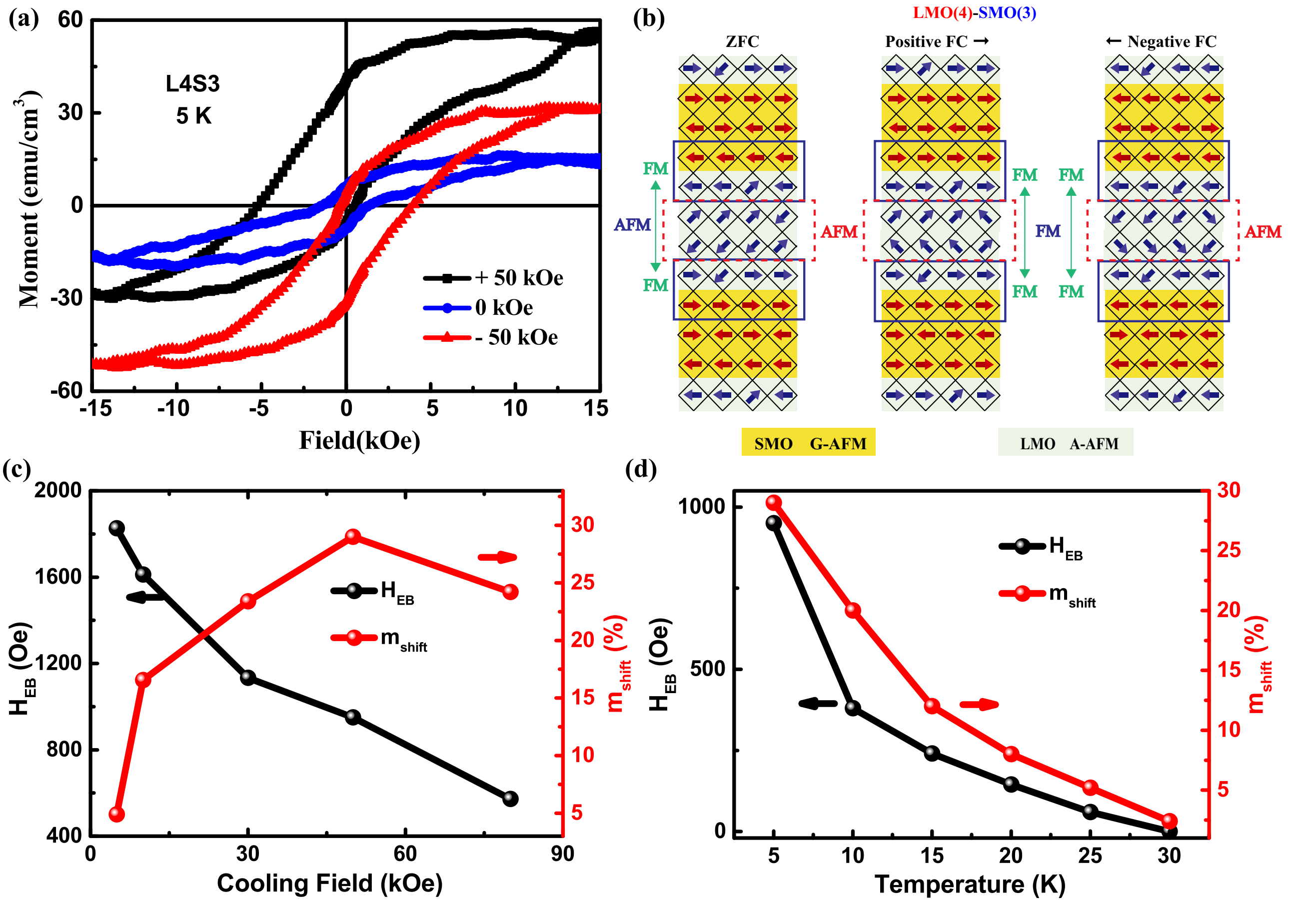

FIG. 6. (a) Magnetic hysteresis loops of the L_4S_3 superlattice measured at 5 K after cooling from room temperature in an in-plane magnetic field of ±50 kOe (red and black) and zero field (blue). (b) Schematic diagrams for local spin configurations at 5 K in the L_4S_3 superlattice after zero-field cooling and ±50 kOe field cooling from room temperature. (c) Dependence of H_{EB} (left axis) and m_{shift} (right axis) on the cooling field, measured at 5 K on the L_4S_3 superlattice. (d) Temperature dependence of H_{EB} (left axis) and m_{shift} (right axis) after cooling in a field of 50 kOe for the L_4S_3 superlattice.

competes with the canted AFM states in the LMO layers, resulting in the coexistence of the EBE and VMS phenomena in the intermediate-period LMO/SMO superlattices. The competition between the underlying canted AFM states and the interfacial FM states is also the origin of the large negative MR effect observed in the L_4S_3 superlattice.

In order to further investigate the complex magnetic structure in the LMO/SMO superlattices, the magnetic structure in the L_4S_3 superlattice has been studied. Figure 6(a) presents the magnetic hysteresis loops of the L_4S_3 superlattice measured at 5 K after being cooled from room temperature with and without the application of an in-plane magnetic field of ±50 kOe. Similar magnetic hysteresis loops for the other L_nS_{n-1} superlattices measured at 5 K are shown in Fig. S6 of the Supplemental Material [38] for comparison. Remarkably, the zero-field-cooling *M-H* loop shows a symmetric hysteresis centered at the origin; in contrast, the field-cooled loops show both the EBE and the VMS. The coexistence of the EBE and the VMS in the L_4S_3 superlattice can be attributed to the competition between the interfacial FM states and the interlayer canted AFM states. In addition, the loops after field cooling show larger saturation magnetizations than the loops after zero-field cooling; the reason for this M_S enhancement is explained in the next section.

Figure 6(b) presents schematic diagrams that show the difference of the spin configurations in the L_4S_3 superlattice after the zero-field-cooling and field-cooling processes. It is generally considered that the FM states in the interface always exist due to the double-exchange effect. However, the neighboring interfacial FM regions are separated by AFM regions, which leads to the AFM exchange coupling of the interfacial FM regions and a more stable spin configuration [see the middle graph in Fig. 6(b)]. When the superlattice is cooled from room temperature under a sufficiently strong magnetic field, the neighboring interfacial FM regions should tend to have a parallel arrangement, while the AFM states in the "bulk" have the preferential canted spin along the direction of the cooling field. This leads to an increased saturation magnetization for the field opposite to the cooling field direction, resulting in the VMS phenomenon.

In order to confirm the dominate role of the competition between the interfacial FM state and the interlayer AFM state for emergent magnetic properties, a nonmagnetic $SrTiO_3$ spacer layer is inserted into each interface of the L_4S_3 superlattice. Typical magnetic hysteresis loops measured with an in-plane field at 5 K with and without a field-cooling process are shown in Fig. S8 of the Supplemental Material [38]. The EBE and VMS behaviors are quickly suppressed with an increase in the STO spacer thickness. This clearly suggests that the competition between the underlying AFM states and the interfacial FM states plays an important role for the emergent magnetic property.

Figure 6(c) shows the dependence of H_{EB} and m_{shift} on the cooling field for the $\mathrm{L_4S_3}$ superlattice. One can see that the cooling field strongly affects H_{EB} and m_{shift}. H_{EB} decreases monotonically with the cooling field. In contrast, with an increase in the cooling field, m_{shift} initially rises sharply and reaches the maximal value at 50 kOe. This evolution of m_{shift} against the cooling field reveals that the relative fraction of the pinned moments is at its largest at 50 kOe, which is in fact the right magnetic field used to cool the $\mathrm{L}_n\mathrm{S}_{n-1}$ superlattices. Figure 6(d) shows the temperature dependence of H_{EB} and m_{shift} for the $\mathrm{L_4S_3}$ superlattice. One can immediately see that the giant EBE and VMS responses take place below 30 K. The largest H_{EB} and m_{shift} values are 950 Oe and 29%, respectively, which were measured at 5 K under a cooling field of 50 kOe.

IV. CONCLUSIONS

In summary, measurements of electrical transport and magnetic properties, along with x-ray linear dichroism, are carried out on $(\mathrm{LMO})_n/(\mathrm{SMO})_{n-1}$ superlattices. The superlattices undergo a metal-to-insulator transition with an increase in the thickness n from 2 u.c. to 8 u.c. Significant exchange bias effects accompanied by large vertical magnetization shifts are observed in the $\mathrm{L_3S_2}$, $\mathrm{L_4S_3}$, and $\mathrm{L_5S_4}$ superlattices. Further, a large nontrivial negative magnetoresistance of 58% is observed in the $\mathrm{L_4S_3}$ superlattice. These emergent magnetic results can be attributed to the competition of the ferromagnetic and antiferromagnetic states in the LMO/SMO superlattices. Due to the spin-orbital coupled states arising in manganites, the spin configurations of FM and AFM phases can be evaluated by x-ray linear dichroism measurements at the Mn L edges. Finally, a spin configuration model is proposed that takes into account complex competition between the interfacial ferromagnetism and the underlying canted antiferromagntism in the superlattices. The model explains the observed transport and magnetic properties.

ACKNOWLEDGMENTS

This work is financially supported by National Natural Science Foundation of China (Grants No. 51901118, No. 51871137, No. 61434002, and No. 51025101) and the Special Funds of Sanjin Scholars Program. We thank Wensheng Yan for the XAS measurement at beamline BL12-a in National Synchrotron Radiation Laboratory (NSRL) and XLD measurement at beamline BL08U1A in Shanghai Synchrotron Radiation Facility (SSRF).

---

[1] H. Y. Hwang, Y. Iwasa, M. Kawasaki, B. Kiemer, N. Nagaosa, and Y. Tokura, Nat. Mater. **11**, 103 (2012).

[2] J. Chakhalian, J. W. Freeland, A. J. Millis, C. Panagopoulos, and J. M. Rondinelli, Rev. Mod. Phys. **86**, 1189 (2014).

[3] J. H. Ngai, F. J. Walker, and C. H. Ahn, Annu. Rev. Mater. Res. **44**, 1 (2014).

[4] A. Ohtomo and H. Y. Hwang, Nature (London) **427**, 423 (2004).

[5] A. Ohtomo, D. A. Muller, J. L. Granzul, and H. Y. Hwang, Nature (London) **419**, 378 (2002).

[6] I. Marozau, P. T. Das, M. Dobeli, J. G. Storey, M. A. Uribe-Laverde, S. Das, C. Wang, M. Rossle, and C. Bernhard, Phys. Rev. B **89**, 174422 (2014).

[7] S. J. May, T. S. Santos, and A. Bhattacharya, Phys. Rev. B **79**, 115127 (2009).

[8] C. W. Lin, S. Okamoto, and A. J. Millis, Phys. Rev. B **73**, 041104(R) (2006).

[9] T. Koida, M. Lippmaa, T. Fukumura, K. Itaka, Y. Matsumoto, M. Kawasaki, and H. Koinuma, Phys. Rev. B **66**, 144418 (2002).

[10] S. Smadici, P. Abbamonte, A. Bhattacharya, X. F. Zhai, B. Jiang, A. Rusydi, J. N. Eckstein, S. D. Bader, and J. M. Zuo, Phys. Rev. Lett. **99**, 196404 (2007).

[11] H. B. Zhao, K. J. Smith, Y. Fan, G. Lupke, A. Bhattacharya, S. D. Bader, M. Warusawithana, X. Zhai, and J. N. Eckstein, Phys. Rev. Lett. **100**, 117208 (2008).

[12] A. Bhattacharya, S. J. May, S. G. E. te Velthuis, M. Warusawithana, X. Zhai, B. Jiang, J. M. Zuo, M. R. Fitzsimmons, S. D. Bader, and J. N. Eckstein, Phys. Rev. Lett. **100**, 257203 (2008).

[13] D. J. Huang, W. B. Wu, G. Y. Guo, H.-J. Lin, T. Y. Hou, C. F. Chang, C. T. Chen, A. Fujimori, T. Kimura, H. B. Huang, A. Tanaka, and T. Jo, Phys. Rev. Lett. **92**, 087202 (2004).

[14] C. Aruta, C. Adamo, A. Galdi, P. Orgiani, V. Bisogni, N. B. Brookes, J. C. Cezar, P. Thakur, C. A. Perroni, G. D. DeFilippis, V. Cataudella, D. G. Schlom, L. Maritato, and G. Ghiringhelli, Phys. Rev. B **80**, 140405(R) (2009).

[15] H. Yamada, P. H. Xiang, and A. Sawa, Phys. Rev. B **81**, 014410 (2010).

[16] A. Galdi, C. Aruta, P. Orgiani, C. Adamo, V. Bisogni, N. B. Brookes, G. Ghiringhelli, D. G. Schlom, P. Thakur, and L. Maritato, Phys. Rev. B **85**, 125129 (2012).

[17] H. Nakao, T. Sudayama, M. Kubota, J. Okamoto, Y. Yamasaki, Y. Murakami, H. Yamada, A. Sawa, and K. Iwasa, Phys. Rev. B **92**, 245104 (2015).

[18] S. Paul, R. Pankaj, S. Yarlagadda, P. Majumdar, and P. B. Littlewood, Phys. Rev. B **96**, 195130 (2017).

[19] H. Nakao, C. Tabata, Y. Murakami, Y. Yamasaki, H. Yamada, S. Ishihara, and M. Kawasaki, Phys. Rev. B **98**, 245146 (2018).

[20] M. Keunecke, F. Lyzwa, D. Schwarzbach, V. Roddatis, N. Gauquelin, K. Muller-Caspary, J. Verbeeck, S. J. Callori, F. Klose, M. Jungbauer, and V. Moshnyaga, Adv. Funct. Mater. (2019), doi:10.1002/adfm.201808270.

[21] P. Padhan and W. Prellier, Phys. Rev. B **72**, 104416 (2005).

[22] R. Rana, P. Pandey, and D. S. Rana, Appl. Phys. Lett. **104**, 092413 (2014).

[23] R. Rana, P. Pandey, R. P. Singh, and D. S. Rana, Sci. Rep. **4**, 4138 (2014).

[24] A. Mumtaz, K. Maaz, B. Janjua, S. K. Hasanain, and M. F. Bertino, J. Magn. Magn. Mater. **313**, 266 (2007).

[25] M. A. K. Budi, E. B. Glass, N. G. Rudawski, and J. S. Andrew, J. Mater. Chem. C **5**, 8586 (2017).

[26] Y. Shiratsuchi, H. Noutomi, H. Oikawa, T. Nakamura, M. Suzuki, T. Fujita, K. Arakawa, Y. Takechi, H. Mori,

T. Kinoshita, M. Yamamoto, and R. Nakatani, Phys. Rev. Lett. **109**, 077202 (2012).

[27] S. J. Yuan, L. Li, T. F. Qi, L. E. DeLong, and G. Cao, Phys. Rev. B **88**, 024413 (2013).

[28] Q. X. Zhu, M. Zheng, M. M. Yang, R. K. Zheng, Y. Wang, X. M. Li, and X. Shi, Appl. Phys. Lett. **105**, 241604 (2014).

[29] S. R. Singamaneni, W. Fan, J. T. Prater, and J. Narayan, J. Appl. Phys. **117**, 17B711 (2015).

[30] P. Pandey, T. Das, R. Rana, J. B. Parmar, S. Bhattacharyya, and D. S. Rana, Nanoscale **7**, 3292 (2015).

[31] Y. J. Wu, Z. J. Wang, Y. Bai, Y. M. Liang, X. K. Ning, Q. Wang, W. Liu, and Z. D. Zhang, J. Mater. Chem. C **7**, 6091 (2019).

[32] M. Zheng and W. Wang, ACS Appl. Mater. Interfaces **8**, 14012 (2016).

[33] M. Zheng, X. Y. Li, W. Xiao, W. Wang, and H. Ni, Appl. Phys. Lett. **111**, 152405 (2017).

[34] M. Ziese, F. Bern, and I. Vrejoiu, J. Appl. Phys. **113**, 063911 (2013).

[35] Q. L. He, X. F. Kou, A. J. Grutter, G. Yin, L. Pan, X. Y. Che, Y. X. Liu, T. X. Nie, B. Zhang, S. M. Disseler, B. J. Kirby, W. Ratcliff, Q. M. Shao, K. Murata, X. D. Zhu, G. Q. Yu, Y. B. Fan, M. Montazeri, X. D. Han, J. A. Borchers, and K. L. Wang, Nat. Mater. **16**, 94 (2017).

[36] G. W. Zhou, H. H. Ji, J. Zhang, Y. H. Bai, Z. Y. Quan, and X. H. Xu, J. Mater. Chem. C **6**, 582 (2018).

[37] G. W. Zhou, H. H. Ji, Y. H. Bai, Z. Y. Quan, and X. H. Xu, Sci. China Mater. **7**, 1046 (2019).

[38] See Supplemental Material at http://link.aps.org/supplemental/10.1103/PhysRevB.101.024422 for the results of high-resolution STEM images, temperature dependence of resistance, magnetic and transport properties, schematic diagrams of local spin orientation, *M*-*H* loops along the in-plane and out-of-plane axes, and *M*-*H* loops for the L4-STO(1)-S3, L4-STO(2)-S3, and L4-STO(3)-S3 superlattices.

[39] M. Gibert, M. Viret, A. Torres-Pardo, C. Piamonteze, P. Zubko, N. Jaouen, J.-M. Tonnerre, A. Mougin, J. Fowlie, S. Catalano, A. Gloter, O. Stephan, and J.-M. Triscone, Nano Lett. **15**, 7355 (2015).

[40] H. Ohldag, A. Scholl, F. Nolting, E. Arenholz, S. Maat, A. T. Young, M. Carey, and J. Stohr, Phys. Rev. Lett. **91**, 017203 (2003).

[41] R. K. Zheng, G. H. Wen, K. K. Fung, and X. X. Zhang, J. Appl. Phys. **95**, 5244 (2004).

[42] S. Thota, S. Ghosh, S. Nayak, D. C. Joshi, P. Pramanik, K. Roychowdhury, and S. Das, J. Appl. Phys. **122**, 124304 (2017).

[43] P. Pandey, R. Rana, and D. S. Rana, Europhys. Lett. **109**, 38005 (2015).

[44] G. W. Zhou, Z. Yan, Y. H. Bai, J. L. Zang, Z. Y. Quan, S. F. Qi, and X. H. Xu, ACS Appl. Mater. Interfaces **9**, 39855 (2017).

[45] D. Pesquera, G. Herranz, A. Barla, E. Pellegrin, F. Bondino, E. Magnano, F. Sanchez, and J. Fontcuberta, Nat. Commun. **3**, 1189 (2012).